Gold nanoshell-localized photothermal ablation of prostate tumors in a clinical pilot device study

Ardeshir R. Rastinehad[a,b,1], Harry Anastos[a], Ethan Wajswol[a], Jared S. Winoker[a], John P. Sfakianos[a], Sai K. Doppalapudi[a], Michael R. Carrick[b], Cynthia J. Knauer[a], Bachir Taouli[b], Sara C. Lewis[b], Ashutosh K. Tewari[a], Jon A. Schwartz[c], Steven E. Canfield[d], Arvin K. George[e], Jennifer L. West[f], and Naomi J. Halas[g,1]

[a]Department of Urology, Icahn School of Medicine at Mount Sinai, New York, NY 10029; [b]Department of Radiology, Icahn School of Medicine at Mount Sinai, New York, NY 10029; [c]Clinical Research, Nanospectra Biosciences, Inc., Houston, TX 77054; [d]Department of Urology, McGovern Medical School at the University of Texas Health Science Center at Houston, Houston, TX 77030; [e]Department of Urology, Michigan Medicine University of Michigan, Ann Arbor, MI 48109; [f]Department of Biomedical Engineering, Duke University, Durham, NC 27708; and [g]Laboratory for Nanophotonics, Rice University, Houston, TX 77005

Edited by Catherine J. Murphy, University of Illinois at Urbana–Champaign, Urbana, IL, and approved July 25, 2019 (received for review April 23, 2019)

Biocompatible gold nanoparticles designed to absorb light at wavelengths of high tissue transparency have been of particular interest for biomedical applications. The ability of such nanoparticles to convert absorbed near-infrared light to heat and induce highly localized hyperthermia has been shown to be highly effective for photothermal cancer therapy, resulting in cell death and tumor remission in a multitude of preclinical animal models. Here we report the initial results of a clinical trial in which laser-excited gold-silica nanoshells (GSNs) were used in combination with magnetic resonance–ultrasound fusion imaging to focally ablate low-intermediate-grade tumors within the prostate. The overall goal is to provide highly localized regional control of prostate cancer that also results in greatly reduced patient morbidity and improved functional outcomes. This pilot device study reports feasibility and safety data from 16 cases of patients diagnosed with low- or intermediate-risk localized prostate cancer. After GSN infusion and high-precision laser ablation, patients underwent multiparametric MRI of the prostate at 48 to 72 h, followed by postprocedure mpMRI/ultrasound targeted fusion biopsies at 3 and 12 mo, as well as a standard 12-core systematic biopsy at 12 mo. GSN-mediated focal laser ablation was successfully achieved in 94% (15/16) of patients, with no significant difference in International Prostate Symptom Score or Sexual Health Inventory for Men observed after treatment. This treatment protocol appears to be feasible and safe in men with low- or intermediate-risk localized prostate cancer without serious complications or deleterious changes in genitourinary function.

MRI-ultrasound fusion | photothermal therapy | focal therapy | gold nanoshell | prostate cancer

Gold nanoparticles absorb light intensely, giving rise to the vivid optical coloration of stained glass windows popularized during medieval times, a property now known as collective electronic excitation or plasmon resonance. Faraday observed that colloidal gold absorbed green light, a system that served as a demonstration of classical electromagnetic theory (1). It was subsequently predicted that hollow gold nanoparticles could substantially shift resonances to longer wavelengths than solid gold nanoparticles, with a resonant frequency controlled by the spherical shell dimensions (2, 3). This was the predictive model for dielectric-core metallic-shell nanoparticles known as nanoshells, first realized in Au_2S-Au and then SiO_2-Au materials (gold-silica nanoshells; GSNs) (4–6). Varying the relative dimension of the inner and outer radius of the gold shell tunes the plasmon resonance, and therefore the wavelength of light absorbed by the particle (7). Tuning the plasmon resonance beyond the visible and into the near-infrared region of the spectrum, a region of high tissue transparency, opened the door to a wide range of applications in nanomedicine (8, 9).

Near-infrared nanomedicine spans diagnostics, such as probe-based imaging of tumor margins, as well as therapeutics, such as remotely triggerable drug or gene delivery. One of the most promising light-based therapeutic modalities is targeted photothermal cancer therapy (10). GSNs (AuroShells) are composed of a silica core and a gold shell with a total diameter of ∼150 nanometers, and are designed to maximally absorb near-infrared light and convert it to heat (10–12). In this therapy, near-infrared-absorbing nanoparticles accumulate in tumor tissue via leaky tumor vasculature, and then are irradiated with a near-infrared laser. The tumor undergoes photothermal heating, resulting in selective hyperthermic cell death, without heating the adjacent nontumorous tissue. Previously, this treatment has been demonstrated extensively in cell studies and in animal models (11–15). Other near-infrared-absorbing nanoparticles such as nanorods, nanocages, and nanostars have also been used in animal studies (16). Preclinical safety has

Significance

Prostate cancer is the most common nonskin cancer in the United States, where approximately 1 in 9 men will be diagnosed in their lifetime. The prostate is near several vital structures, such as the urethra and neurovascular bundle, and whole gland treatments for prostate cancer can disrupt normal urinary, bowel, and sexual functioning. Here we report the initial results of a clinical trial for nanoparticle-based photothermal cancer therapy. The trial was designed to perform ultrafocal photothermal ablation of cancerous tumors within the prostate. Gold-silica nanoparticles designed to absorb near-infrared light at wavelengths of high tissue transparency provide a highly localized light-based strategy for the treatment of prostate cancer, with substantially reduced risks for deleterious treatment-related side effects.

Author contributions: A.R.R. invented the transperineal MR US fusion guided gold nanoshell excitation technique used in the trial; A.R.R., J.A.S., J.L.W., and N.J.H. designed research; A.R.R., H.A., E.W., J.S.W., J.P.S., S.K.D., M.R.C., C.J.K., B.T., S.C.L., A.K.T., J.A.S., S.E.C., A.K.G., J.L.W., and N.J.H. performed research; J.A.S., J.L.W., and N.J.H. contributed new reagents/analytic tools; A.R.R., H.A., E.W., J.S.W., J.P.S., S.K.D., M.R.C., C.J.K., B.T., S.C.L., A.K.T., S.E.C., and A.K.G. analyzed data; and A.R.R., H.A., E.W., J.S.W., J.P.S, S.K.D., M.R.C., C.J.K., B.T., S.C.L., A.K.T., J.A.S., S.E.C., A.K.G., J.L.W., and N.J.H. wrote the paper.

Conflict of interest statement: A.R.R. is the national principal investigator for the multi-institutional trial of GSN-directed ablation, funded by Nanospectra Biosciences. He is also a consultant for Nanospectra Biosciences. J.L.W. and N.J.H. cofounded Nanospectra Biosciences in 2001 to transfer the photothermal therapeutics process from their labs into the clinic. They both have a small equity stake in this company but are not involved in any way with the company's business or strategic decisions.

This article is a PNAS Direct Submission.

[1]To whom correspondence may be addressed. Email: art.rastinehad@mountsinai.org or halas@rice.edu.

This article contains supporting information online at www.pnas.org/lookup/suppl/doi:10.1073/pnas.1906929116/-/DCSupplemental.

Published online August 26, 2019.

been established for AuroShell particles in vitro and in vivo in animal testing (17, 18).

Prostate cancer is the most commonly diagnosed cancer and the second leading cause of cancer deaths in men. In 2019, it is estimated there will be 31,620 deaths caused by prostate cancer in the United States (19). Multiparametric high-resolution MR imaging (mpMRI) of the prostate has provided urologists with the ability to observe, target, and stage patients at risk for prostate cancer. Along with technological advances, the trend toward overtreatment of prostate cancer with whole gland treatments has highlighted a need for better focal therapies with fewer complications. In an analysis from the University College London evaluating patients postprostatectomy, researchers reported that up to 51% of patients could have been considered candidates for focal prostate ablation of their index lesion (20).

The underlying rationale for focal prostate ablation is the treatment of localized prostate cancer while minimizing the side effects associated with whole gland treatments, which can include urinary incontinence and erectile dysfunction (21–25). Various focal ablation modalities have been investigated, with promising short-term oncological and functional outcomes. These include cryotherapy, high-intensity focused ultrasound, laser interstitial thermal therapy (LITT), irreversible electroporation, and photodynamic therapy (26–32). The combination of mpMRI with MR/US fusion biopsy platforms has greatly enhanced the ability to identify and target suspicious lesions, resulting in improved risk stratification and staging, which results in a decrease in the detection of clinically insignificant disease and an increase in the detection of high-grade prostate cancer (33).

AuroLase Therapy (Nanospectra Biosciences, Inc., Houston, TX) is a focal ablation modality that relies on laser excitation of GSN to selectively target and treat focal lesions within the prostate. Intravenously delivered GSNs preferentially accumulate within solid tumor tissue due to vessel wall fenestrations associated with aberrant tumor neovasculature and inherently defective lymphatic drainage within these lesions (18, 34, 35). On illumination with a near-infrared laser at a subablative power, healthy tissue with lower concentrations of GSN experiences mild and reversible hyperthermia, while the higher concentrations of GSN within the cancerous lesion generate sufficient photothermal energy to produce coagulative necrosis (10, 11, 36). Using the inherent properties of GSN tissue distribution, the technology has the potential to provide treatment that produces a self-limited volume of tumor tissue destruction. Selective controlled ablation in the prostate may translate to improved clinical outcomes while minimizing the side effects commonly observed with other focal ablation modalities, primarily due to the ablation of nontargeted tissue, leading to subsequent complications such as urethral fistula, urinary incontinence, erectile dysfunction, and/or rectal injuries.

A prior treat-and-resect study evaluating the safety of AuroLase Therapy was successfully completed, assessing for adverse reactions associated with the infusion of GSN and subsequent nontarget transrectal ultrasound-guided laser excitation of a single lobe of the prostate in patients undergoing radical prostatectomy (18). After demonstrating a reasonable side effect profile, we sought to take the next step and assess AuroLase Therapy using an MR/US transperineal fusion biopsy platform. In this pilot study approved by the institutional review board (Biomedical Research Alliance of New York) under FDA IDE clearance, we collected feasibility and safety data of focal GSN-mediated laser ablation. The primary safety endpoint of this trial was the absence of any grade 3 adverse events as classified by Common Terminology Criteria for Adverse Events (CTCAE) version 5. Additional endpoints included changes in genitourinary function compared with baseline, as well as treatment efficacy confirmed by pathology at 3 and 12 mo, determined by follow-up MR/US fusion biopsy of the ablation site.

Results

Fifteen of the initial 16 patients successfully completed the treatment protocol. One patient (#3) experienced transient epigastric pain during the GSN infusion and did not undergo day 2 laser treatment. During each procedure, a median of 11 (range, 4 to 21) trocars were inserted, which correlated to the cross-sectional area of the tumor in the axial plane. The median number of laser excitations was 25 (range, 5 to 52). The laser power used was increased from 4.5 W up to 6.5 W on switching to a longer, 18-mm, optical fiber diffuser (OFD; after patient #3) due to dosimetry adjustments required for the lengthened geometry of the laser ablation zone. The median time under anesthesia, including patient positioning and equipment preparation, was 230 min (range, 115 to 345). Treatment attributes are summarized in *SI Appendix*, Table S1.

Median prostate volume observed on MRI decreased from 49 cm^3 at baseline to 42 cm^3 at 3 mo (Wilcoxon signed-rank test $P = 0.23$). Median prostate-specific antigen (PSA) at baseline decreased from 6.7 ng/mL at baseline to 3.9 ng/mL at 3 mo (Wilcoxon signed-rank test $P < 0.01$). Median PSA density decreased from 0.137 ng/cm^2 at baseline to 0.083 ng/cm^2 at 3 mo (Wilcoxon signed-rank test $P < 0.01$). Baseline and follow-up PSA at 3, 6, and 12 mo are charted in Fig. 1.

There were no serious adverse events (CTCAE grade 3 or greater) during the procedure, and all patients were discharged home the day of the procedure. Patient #1 was discharged with a Foley catheter. All subsequent patients were given the opportunity to void before discharge, and 4 additional patients required a Foley catheter postablation. A patient (#10) reported ventral bending of the distal third of the penis during erections at the 12-mo visit. This most likely was due to the use of the Foley catheter during the procedure. As previously mentioned, there was a transient CTCAE grade 1 to 2 substernal epigastric pain during GSN infusion, which was attributed to the cold temperature of the GSN suspension taken directly from the storage refrigerator. In all subsequent cases, the suspension was given time to reach room temperature. All adverse events reported within the 90-d posttreatment period are listed in *SI Appendix*, Table S2.

The median International Prostate Symptom Score (IPSS) at baseline, 1 mo, 3 mo, 6 mo, and 12 mo was 8, 9, 8, 8, and 8, respectively. Median IPSS between baseline and 3-mo follow-up was not significantly different (Wilcoxon signed-rank test $P = 0.06$). Urinary QoL at baseline, 1 mo, 3 mo, 6 mo, and 12 mo was 2, 2, 1, 1, and 2, respectively, with no statistical difference between baseline and 3 mo follow-up (Wilcoxon signed-rank test $P = 0.33$). In sexually active patients, the median Sexual Health Inventory for Men (SHIM) score (with or without phosphodiesterase-5 inhibitor therapy) at baseline, 1 mo, 3 mo, 6 mo, and 12 mo was 23.5, 21, 21.5, 22, and 20.50, respectively, with no statistical difference between baseline and 3 mo follow-up (Wilcoxon signed-rank test $P = 0.10$). A boxplot of IPSS, urinary QoL, and SHIM at baseline, 1 mo, 3 mo, 6 mo, and 12 mo is illustrated in Fig. 2.

Results from mpMRI at 48 to 72 h and 3 mo after treatment are shown in Fig. 3. At 48 to 72 h, T2-weighted imaging and DWI both demonstrated edema and nonspecific changes within the ablated area. DCE-MRI demonstrated an adequate ablation zone in all but 2 patients; patient #6, who had residual enhancement at the anterior distal ablation zone, and patient #10, who had rim enhancement at the distal ablation zone.

At 3 mo, all patients had evidence of contraction and scar formation at the former ablation zones on T2-weighted imaging, and nonspecific changes on DWI. DCE-MRI sequences demonstrated a complete loss of enhancement within the intended ablation zones of most patients (Fig. 3). Patients #2 and #7 had new areas of enhancement at the proximal portions of their respective ablation zones that were suspicious for persistent disease. These

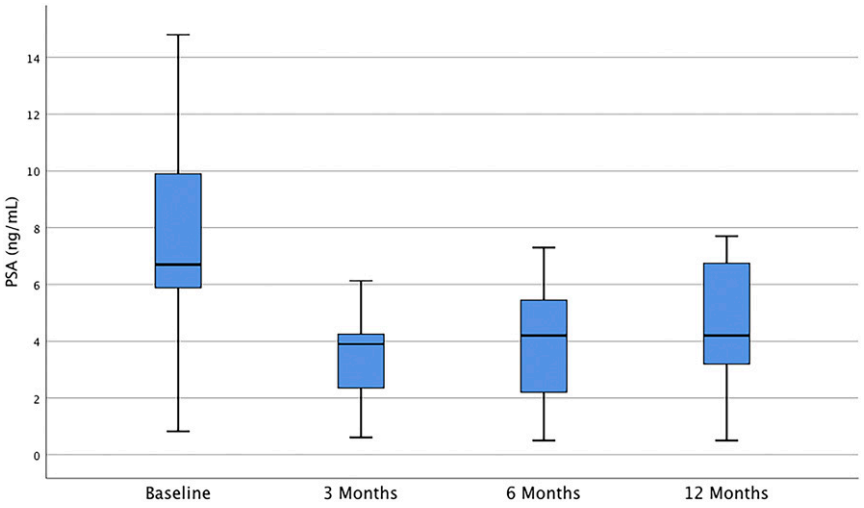

Fig. 1. Boxplot comparing PSA(ng/ml) at baseline, 3, 6, and 12 mo after treatment. Wilcoxon signed ranks test compared with baseline PSA(ng/ml) at 3 mo ($P = 0.001$), at 6 mo ($P = 0.002$), and at 12 mo ($P = 0.002$).

imaging findings correlated with residual disease on follow-up targeted biopsy at 3 mo. Representative MRI images of the prostate pretreatment and 3-mo posttreatment are shown in Fig. 3.

All 15 treated patients with 16 total lesions underwent mpMRI and targeted biopsy at 3 mo, as well as a mpMRI, targeted biopsy, and systematic 12 core standard biopsy at 12 mo posttreatment. Depending on the size of the lesion, a total of 3 to 6 targeted cores were obtained. All patients had evidence of coagulative necrosis on repeat biopsy. The ablation zones were negative for tumor in 62.5% (10/16) of lesions at 3 mo. At 12 mo, 87.5% (14/16) of lesions were negative for tumor in the ablation zones. Per Delphi consensus definition of clinically significant PCA, 75% (12/16) of treatment outcomes were considered successful at 3 mo, and 87.5% (14/16) at 12 mo. The conversion of the 3-mo positive biopsy to a negative biopsy at 12 mo could be due to undersampling of the targeted region. However, other investigators have also postulated that time is required for resolution of the inflammatory response, and this could also be associated with an abscopal effect postablation that can take up to 6 mo (37). Table 1 summarizes the 3-mo and 12-mo targeted biopsy results.

After laser illumination, a core of tumor was sampled and assayed for GSN concentration from 14 patients (15 tumors). These samples were submitted for elemental analysis, which quantified the mass of gold in each sample. The mean concentration of gold in the sampled tumors was 8.28 μg/g (range, 1.15 to 33.12 μg/g), corresponding to 4.24e8 GSN/mL (range, 0.78 to 22.60e8 GSN/mL) due to 88% of an AuroShell being composed of gold by mass.

Discussion

The landscape of prostate cancer therapy has evolved dramatically during the last decade, with growing interest in and the investigation of various focal ablation technologies. Laser ablation devices have obtained FDA approval for soft tissue ablation (38, 39). Compared with other focal ablation treatment modalities, laser ablation has the advantage of generating accurate, predictable, and homogeneous ablation without causing collateral damage

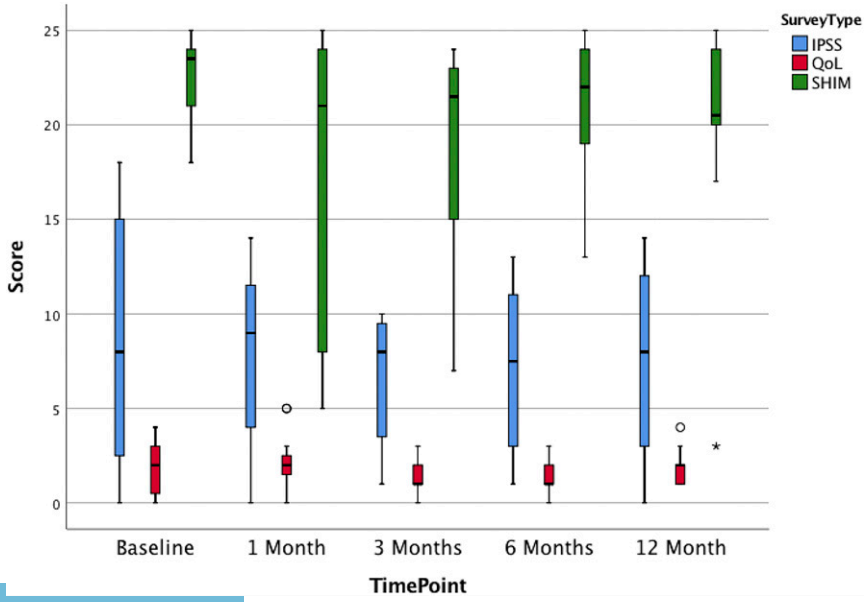

Fig. 2. Boxplot comparing International Prostate Symptom Score, urinary quality of life, and Sexual Health Inventory for Men scores at baseline, 1, 3, 6, and 12 mo.

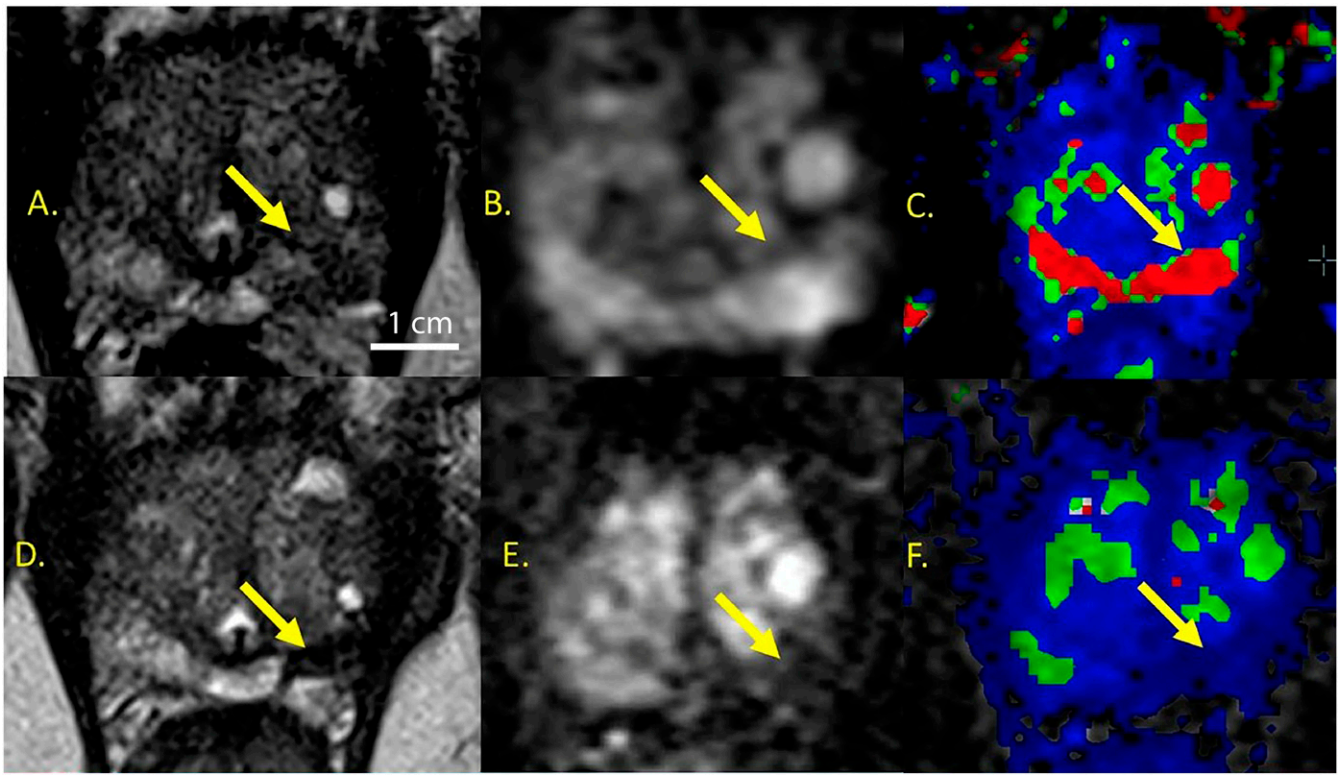

Fig. 3. Representative case of a 70-y-old man with focal prostate cancer treated successfully with GSN-directed laser excitation and ablation (*A*–*C*) pretreatment, (*D* and *E*) 3 mo posttreatment. Follow-up biopsy at 3 mo was negative for cancer. (*A*) Axial T_2-weighted image demonstrating left apex tumor Gleason 3+4 on targeted biopsy (arrow). (*B*) DWI image for b = 2,000 demonstrates restricted diffusion in tumor (hyperintensity compared to normal peripheral zone). (*C*) DCE-MRI parametric map (Ktrans/Ve) demonstrates increased enhancement of the tumor. (*D*) Axial T_2-weighted image after treatment demonstrating contraction of ablation zone, appearing markedly hypointense, compatible with hemorrhagic/necrotic changes. (*E*) DWI image for b = 2,000 demonstrates resolution of restricted diffusion in treated tumor (arrow). (*F*) DCE-MRI parametric map (Ktrans/Ve) demonstrates resolution of abnormal enhancement in treated tumor (arrow). (Scale bar: 1 cm.)

to adjoining critical structures (40). GSN-directed ablation builds on the initial lessons learned from LITT, attempting to overcome some of the known limitations of laser ablative technology. LITT relies on in-bore MR thermometry or thermocouples to monitor temperatures within the target and surrounding tissues. However, based on review of recent medical device reports and reported adverse events in the neurosurgical literature, the FDA has issued a warning of risk of overheating with laser ablation, possibly due to inaccurate MR thermometry (41). GSN-directed ablation is able to overcome this limitation of available LITT devices by using subablative laser energies with the preferential intratumor accumulation and photothermal properties of GSN. This gives the theoretical advantage of allowing wider ablation margins to ensure adequate lesion coverage, while at the same time allowing successful ablation of only the GSN-concentrated tissue within the laser ablation zone.

Our current pilot study met its primary safety endpoint of the lack of any CTCAE grade 3 or higher adverse events at 90 d follow-up. In addition, no significant change was observed between baseline and 3-mo IPSS, QoL, and SHIM after treatment. Due to the novelty of the technology, it is difficult to find similar therapies against which to evaluate the relative safety and tolerability of GSN-mediated laser ablation. The closest technology that can serve as a comparator is MRI-guided LITT. In a study of 25 men undergoing MRI-guided focal LITT for prostate cancer conducted by Lepor et al. (42), no significant changes in IPSS or SHIM were noted at 3 mo of follow-up, mirroring the results found in the present study. In a different trial of 27 men undergoing MRI-guided LITT by Oto et al. (43), no CTCAE grade 3 adverse events occurred and IPSS did not change after treatment; however, there was a significant decrease in SHIM at 1 and 3 mo that resolved at 12 mo. Regarding the endpoint of assessing efficacy within our current study, the ablation zones were free of cancer in 60% (9/15) of patients at 3 mo and 86.7% (13/15) of patients at 12 mo. These efficacy results are similar to those reported in MRI-guided LITT, with 89% having a negative ablation zone targeted biopsy at 12 mo (44).

Although treatment failures were low, several reasons may explain these circumstances within the current study. Two occurrences of residual disease on 3-mo biopsy (patient #6 and patient #7) appear attributable to the positioning of the laser catheter, resulting in overestimation of laser energy penetration at the distal tip of the optical fiber diffuser. As a result, we presumed the laser energy was not delivered to the entire lesion. At 12 mo, the MRI of patient #6 demonstrated a small focal area of diffusion restriction and enhancement within the treatment cavity, measuring 5 mm. At 12 mo, the MRI of patient #7 demonstrated a mild nodular enhancement along the posterior aspect of the treatment cavity measuring 4 mm. It should be noted that despite these MRI findings, on 12-mo biopsy, both patient #6 and patient #7 had a negative biopsy. It is postulated that the process of necrosis in the underexposed area took longer than in patients who had adequate laser penetration and exposure. Residual disease in patients #2 and #10 at both 3 and 12 mo may be due to incomplete treatment secondary to underestimation of lesion volume during procedural planning. Although patient #10 had a negative targeted biopsy of the ablation zone at 12 mo, a nontargeted core returned as 4+3 GS, measuring 5 mm in length. The nontargeted core overlapped with a previously unrecognized small lesion just medial to the

Table 1. 3- and 12-mo follow-up biopsy results from the targeted ablation zone

	3-mo biopsy results		12-mo biopsy results	
Patient no.	Gleason score	Maximum cancer core length	Gleason score	Maximum cancer core length
1	Negative	—	Negative	—
2	3+3	2.4 mm	3+3	9 mm
3	*	*	*	*
4	Negative	—	Negative	—
5	Negative	—	Negative	—
6	3+3	0.7 mm	Negative	—
7	3+4	5 mm	Negative	—
8	Negative	—	3+4	3 mm
9	Negative	—	Negative	—
10	3+4	5 mm	Negative†	—
11	3+3	4 mm	Negative	—
12	Negative	—	Negative	—
13-A	Negative	—	Negative†	—
13-B	3+4	0.5 mm	Negative†	—
14	Negative	—	Negative	—
15	Negative	—	Negative	—
16	Negative	—	Negative	—

*Patient 3 did not undergo treatment after initial GSN infusion.
†Although the targeted biopsy for these patients was negative, a nontargeted core was positive; for patient 10, a 5-mm core was positive for 4+3 carcinoma, and for patient 13, a 1.5-mm core was positive for 3+4 carcinoma.

ablation zone that was present on retrospective MR image review using information from the 3D mapped prostate biopsy cores. This treatment failure was attributed to the use of outside pretreatment biopsy data and MRI for treatment planning.

To prevent similar treatment failures in the future, we have made cumulative modifications to our technique. The first 3 patients enrolled in the study were treated using a 10-mm OFD (Medtronic UroKit-400-T10). After the treatment of these patients, the laser catheter was replaced with a custom-designed laser catheter incorporating an 18-mm OFD to increase the effective ablation zone longitudinally from 8 mm to 12.5 mm, potentially reducing treatment time by up to 50%. The laser trocars were also placed further into the prostate to decrease undertreatment at the distal tip. Furthermore, the laser power used during the procedures has been adjusted between 5.5 W and 6.5 W, using the 18-mm OFD to maximize GSN-directed ablation while minimizing ablative temperatures in surrounding tissues. Further analysis of ablation zone outcomes is required to optimize the proper energy requirements during GSN-mediated ablation. To prevent treatment failures due to underestimation of tumor volume (such as patient #2 and #10), we have begun meticulously checking lesion segmentation before treatment and favoring the use of in-house biopsy data.

In a study evaluating the safety profile of GSN infusion and laser excitation in men scheduled for radical prostatectomy, the mean concentration of gold (a direct correlate of GSN concentration) in the cancerous areas (16.6 μg/g) was ~3.5 times higher than the concentration in areas of prostate intraepithelial neoplasia (5.8 μg/g), BPH (4.4 μg/g), and normal tissue (4.4 μg/g) (18). In the current study, the median concentration of gold in the sampled tumors was 8.28 μg/g (range, 1.15 to 33.12 μg/g). The observed variability in GSN concentration from our sampled tumors may reflect tumor heterogeneity and/or tissue sampling error. While concentrations in the control areas were not obtained, there is a presumed relative elevation in GSN concentration within the tumor tissue, according to our radiographic findings, confirming selective thermal ablation of the targeted lesions and sparing healthy surrounding tissue from damage (Fig. 4). In the future, we plan to amend the study protocol to include sampling of the control areas before laser excitation to determine the degree of GSN accumulation.

Although the initial results of GSN-mediated laser ablation are promising, the complete results of the multiinstitutional clinical trial ($n = 45$) with 12 mo of follow-up are necessary to establish GSN-mediated laser ablation as an efficacious therapy. The current trial was not powered for all end points (such as efficacy); thus, any interpretation of efficacy remains premature. Additional data analysis would help to determine the optimal candidates for GSN-mediated laser ablation, and cost-effectiveness must be determined in the future. Despite these limitations, the present data justify future exploration and study of GSN-mediated laser ablation as a focal therapy for prostate cancer.

This current pilot device study demonstrates that GSN-directed laser excitation and ablation is a safe and technically feasible procedure for the targeted destruction of prostate tumors.

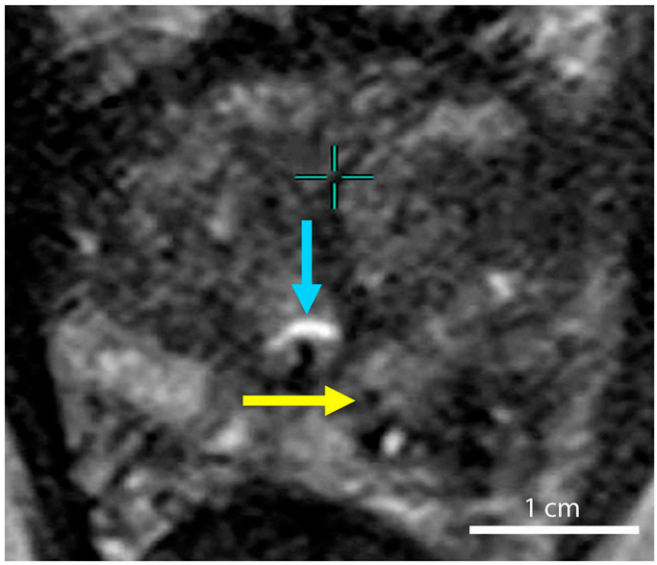

Fig. 4. Axial T_2-weighted image of the prostate with the laser catheter (yellow arrow) within 2 mm of urethra (blue arrow) with sparing of the tissue. (Scale bar: 1 cm.)

Materials and Methods

Nanoshell fabrication was based on the method of Oldenburg (6), and is described in the *SI Appendix*. After synthesis, nanoshells were suspended in 10% trehalose solution to create an iso-osmotic solution for injection, and concentrated by transverse flow filtration to an extinction of 100 ± 5 OD (at 800 nm) to reduce the infused fluid volume. Nanoshells were fabricated under clean conditions in a Class 100 clean room and passed through a 0.45-μm filter before terminal sterilization.

Dosages for AuroShell concentration and light irradiation power levels and exposure times were determined on the basis of data from previous animal and clinical trials (18, 45). The administered AuroShell dose of 7.5 mL/kg was confirmed in an earlier human dose escalation study (17). Details of the dosage and irradiation time determination are described in the *SI Appendix*.

Sixteen men aged 58 to 79 y with clinical stage T2a or less prostate cancer, Gleason score of 4+3 or less, and a minimum postablation follow-up of 12-mo endpoints were analyzed. All patients were diagnosed by MR-US fusion biopsy, including both targeted and systematic sampling, and had discrete MR-visible lesions without other foci of prostate cancer. Systematic sampling refers to the sextant biopsy scheme for the transrectal approach, and the transperineal sampling was performed using a modified Barzel template (all biopsies included a minimum of 12 cores) (46). All patients had a single focus of prostate cancer, with the exception of a single patient who had 2 discrete and separately treated lesions. Complete inclusion and exclusion criteria are listed in the *SI Appendix*. mpMRI was obtained using a 3-Tesla phased array coil and classified using the Prostate Imaging Reporting and Data System version 2 (PI-RADS v2). GSN-mediated laser ablation was performed within 4 mo of mpMRI acquisition. Diagnostic mpMRI studies and fusion biopsies were accepted if performed at another institution; however, all subsequent studies and biopsies were performed at the Mount Sinai Hospital. Initial patient demographics and lesion characteristics are listed in *SI Appendix*, Table S1.

Regions of interest corresponding to the lesions detected on prior MR/US fusion biopsy were marked in preparation for GSN-mediated laser ablation. Region of interest selection and prostatic segmentation were performed, using DynaCAD software (InVivo, A Philips Healthcare Company, Best, Netherlands). An 8- to 10-mm margin of ablation around the target lesion or lesions was marked while avoiding critical nearby structures (e.g., urethra; Fig. 5). Stereotactic trocar/laser fiber placement was planned, using an in-house-generated mockup of a transperineal stepper overlaid on the ablation and tumor regions of interest. To ensure complete coverage of the lesion(s), trocar/laser fiber insertion sites were placed ∼5 to 7 mm apart, considering a 4- to 5-mm treatment radius around the optical fiber diffuser (Fig. 5).

Treatment took place in 2 stages on consecutive days. On treatment day 1, patients received a 7.5 mL/kg i.v. infusion of GSN (4.8 mg/mL) through a standard nonbis(2-ethylhexyl) phthalate infusion set at a rate of 120 to 600 mL/h. Before treatment on day 2, patients received a saline enema and single dose of Gentamicin 160 mg i.v. PB. Patients subsequently underwent laser illumination under general anesthesia while positioned in the dorsal lithotomy position. Periprostatic nerve block was performed using 1% lidocaine without epinephrine under transrectal ultrasound guidance via the perineum. The procedure was performed with continuous cooling irrigation via a 16- or 18-French 3-way urinary catheter.

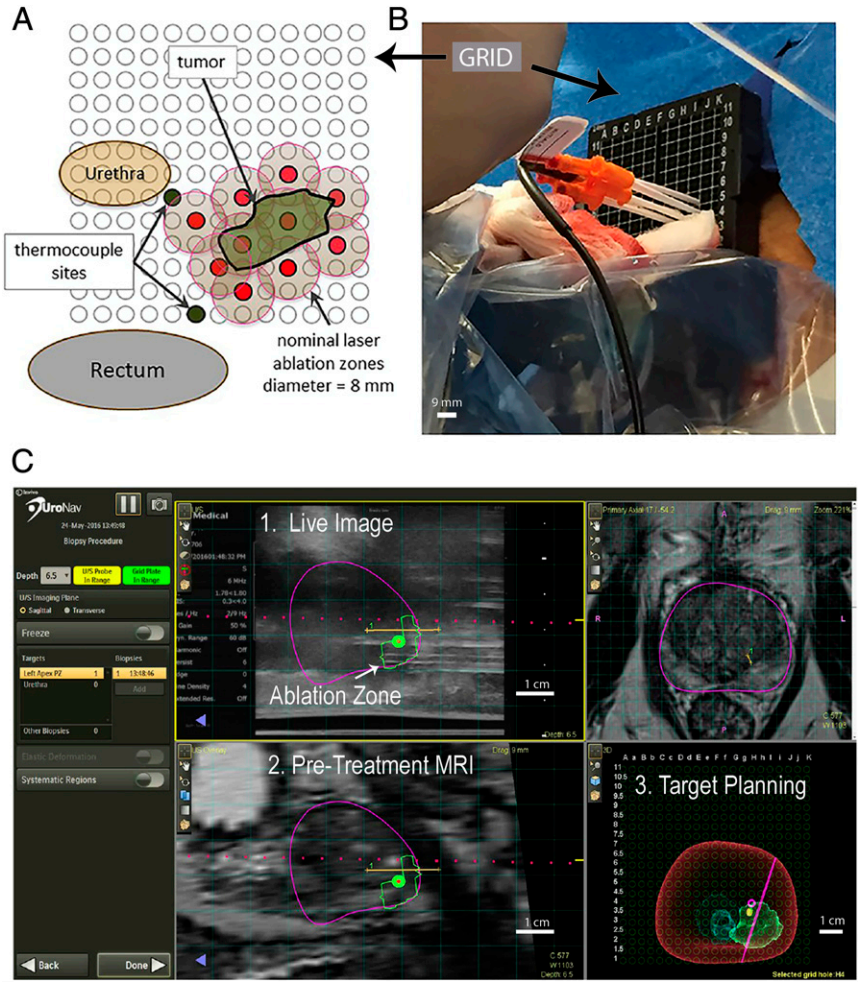

Fig. 5. Transperineal approach. (*A*) An axial view of the prostate ablation zone and the nearby urethra and rectum overlaid with a rectangular transperineal grid (3-mm spacing). The ablation zone is penetrated with the introducer trocars (red) through the targeting grid, allowing for the 4- to 5-mm treatment radius(tan). (*B*) Laser introducers (orange hub) placed with the thermocouple (black) through the transperineal grid. (*C*) UroNav MR/US Fusion guidance for trocar placement with real-time ultrasound imaging. 1. Live US and fusion image in which the purple horizontal line is the planned path for the trocars through the virtual target (ablation zone). 2. Pretreatment MRI denoting the prostate (purple), ablation zone region of interest. 3. Targeting screen allows planning for treatment and trocar placement. (Scale bar: *B*, 9 mm; *C*, 1 cm.)

In conjunction with a biplanar BK ultrasound 8848 probe, 14-gauge grid (CIVCO 610–977), and an EM-tracked MR/US fusion guidance platform with EM compatible stepper (UroNav, A Philips Healthcare company, Best, Netherlands), multiple 14G needle-guided introducers were placed transperineally. Once all introducers were in place, the trocars were removed just before the laser catheter was inserted sequentially into each trocar cannula, and near-infrared light (810 ± 10 nm) was delivered continuously for 3 min at a power level subablative in the absence of GSN. Laser power was delivered via a dual-lumen, water-cooled catheter (Nanospectra Biosciences, Inc., Houston, TX), housing either a 10-mm OFD and power up to 4.5 W or an 18-mm OFD with power up to 6.5 W. Depending on the cranio-caudal dimension of the intended ablation zone, consecutive laser activations took place after withdrawing the laser fiber, to allow for adequate coverage of the intended ablation zone. The specific withdrawal length was dependent on the length of the fiber used for each treatment. An 8-mm withdrawal was used for the 10-mm OFD, and 12-mm withdrawal for the 18-mm OFD. All 3D data were recorded on the MR/US fusion guidance platform (*SI Appendix*, Fig. S1).

To monitor and minimize the risk for tissue damage near critical structures, needle thermocouples were placed near them when the intended ablation zone was in close proximity. This included the urethra, urinary sphincter, and/or rectal wall. As a control treatment, a single 3-min continuous laser excitation with the same laser power was performed at a location contralateral to the target lesion to evaluate whether or not ablation occurred in the absence of GSN.

Patients were discharged on the same day of the procedure after several hours of monitoring and a successful voiding trial. At 48 to 72 h posttreatment, subjects underwent mpMRI to evaluate the radiologic treatment response at the planned ablation zone. Posttreatment follow-up was performed at 1, 3, 6, and 12 mo postablation. At each visit, a history and physical were performed to document any potential adverse events; in addition, patient IPSS and SHIM scores, PSA, and liver function tests were documented. At 3 and 12 mo, patients underwent repeat mpMRI and MR/US targeted biopsy, along with a 12-core systematic biopsy at 12 mo.

Establishment and confirmation of a particle-directed, as opposed to a nonspecific, laser dose was a 2-step process. First, the 6.3 ± 5.8 mg biopsy by mass was taken from the treatment zone to document the presence of nanoshells within each treated tumor (*SI Appendix*, Table S1). An elemental analysis was performed on each biopsy core, using Nuclear Activation Analysis, as previously described (36). Healthy prostate tissue is known to collect a minimal background level of 0.4 μg/g of nanoshells (17). Second, the 48- to 72-h posttreatment DCE MRI helped to establish the volume of target tissue damage before necrotic reformation. This was compared with the minimal thermal ablation zone generated by the control treatment duplicating the laser dose in each patient, and was taken as confirmation that the applied laser dose was specific to tissues containing nanoshells.

The Biomedical Research Alliance of New York Institutional Review Board approved and conducted oversight of trial NBI-PC-002. A data safety and monitoring board also conducted oversight of the clinical trial. The patients were provided with the research consent to review at home and discuss any questions that might arise before signing consent at their next appointment (screening visit). All patients were consented by the principal investigator (A.R.R.).

ACKNOWLEDGMENTS. Nanospectra Biosciences Inc. (Houston, TX) is the primary sponsor of the study providing financial funding for trial. Invivo, a Philips Healthcare Company (Best, Netherlands), provided research equipment support. N.J.H. would like to acknowledge the Welch Foundation (C-1220) for their support.

1. G. Mie, Articles on the optical characteristics of turbid tubes, especially colloidal metal solutions. *Ann. Phys. Berlin* **25**, 377–445 (1908).
2. A. L. Aden, M. Kerker, Scattering of electromagnetic waves from 2 concentric spheres. *J. Appl. Phys.* **22**, 1242–1246 (1951).
3. A. E. Neeves, M. H. Birnboim, Composite structures for the enhancement of nonlinear-optical susceptibility. *J. Opt. Soc. Am. B* **6**, 787–796 (1989).
4. R. D. Averitt, D. Sarkar, N. J. Halas, Plasmon resonance shifts of Au-coated Au2S nanoshells: Insight into multicomponent nanoparticle growth. *Phys. Rev. Lett.* **78**, 4217–4220 (1997).
5. H. S. Zhou, I. Honma, H. Komiyama, J. W. Haus, Controlled synthesis and quantum-size effect in gold-coated nanoparticles. *Phys. Rev. B Condens. Matter* **50**, 12052–12056 (1994).
6. S. J. Oldenburg, R. D. Averitt, S. L. Westcott, N. J. Halas, Nanoengineering of optical resonances. *Chem. Phys. Lett.* **288**, 243–247 (1998).
7. E. Prodan, C. Radloff, N. J. Halas, P. Nordlander, A hybridization model for the plasmon response of complex nanostructures. *Science* **302**, 419–422 (2003).
8. R. Weissleder, A clearer vision for in vivo imaging. *Nat. Biotechnol.* **19**, 316–317 (2001).
9. B. Pelaz *et al*., Diverse applications of nanomedicine. *ACS Nano* **11**, 2313–2381 (2017).
10. L. R. Hirsch *et al*., Nanoshell-mediated near-infrared thermal therapy of tumors under magnetic resonance guidance. *Proc. Natl. Acad. Sci. U.S.A.* **100**, 13549–13554 (2003).
11. S. Lal, S. E. Clare, N. J. Halas, Nanoshell-enabled photothermal cancer therapy: Impending clinical impact. *Acc. Chem. Res.* **41**, 1842–1851 (2008).
12. D. P. O'Neal, L. R. Hirsch, N. J. Halas, J. D. Payne, J. L. West, Photo-thermal tumor ablation in mice using near infrared-absorbing nanoparticles. *Cancer Lett.* **209**, 171–176 (2004).
13. C. Loo *et al*., Nanoshell-enabled photonics-based imaging and therapy of cancer. *Technol. Cancer Res. Treat.* **3**, 33–40 (2004).
14. N. S. Abadeer, C. J. Murphy, Recent progress in cancer thermal therapy using gold nanoparticles. *J. Phys. Chem. C* **120**, 4691–4716 (2016).
15. X. Huang, I. H. El-Sayed, W. Qian, M. A. El-Sayed, Cancer cell imaging and photothermal therapy in the near-infrared region by using gold nanorods. *J. Am. Chem. Soc.* **128**, 2115–2120 (2006).
16. E. C. Dreaden, A. M. Alkilany, X. Huang, C. J. Murphy, M. A. El-Sayed, The golden age: Gold nanoparticles for biomedicine. *Chem. Soc. Rev.* **41**, 2740–2779 (2012).
17. S. C. Gad, K. L. Sharp, C. Montgomery, J. D. Payne, G. P. Goodrich, Evaluation of the toxicity of intravenous delivery of AuroShell particles (gold-silica nanoshells). *Int. J. Toxicol.* **31**, 584–594 (2012).
18. J. M. Stern *et al*., Initial evaluation of the safety of nanoshell-directed photothermal therapy in the treatment of prostate disease. *Int. J. Toxicol.* **35**, 38–46 (2016).
19. R. L. Siegel *et al*., Cancer statistics, 2019. *CA Cancer J Clin* **69**, 7–34 (2019).
20. M. Karavitakis *et al*., Histological characteristics of the index lesion in whole-mount radical prostatectomy specimens: Implications for focal therapy. *Prostate Cancer Prostatic Dis.* **14**, 46–52 (2011).
21. M. Valerio *et al*., The role of focal therapy in the management of localised prostate cancer: A systematic review. *Eur. Urol.* **66**, 732–751 (2014).
22. W. van den Bos *et al*., Focal therapy in prostate cancer: International multidisciplinary consensus on trial design. *Eur. Urol.* **65**, 1078–1083 (2014).
23. M. J. Resnick *et al*., Long-term functional outcomes after treatment for localized prostate cancer. *N. Engl. J. Med.* **368**, 436–445 (2013).
24. F. H. Schröder *et al*.; ERSPC Investigators, Screening and prostate cancer mortality: Results of the European Randomised Study of Screening for Prostate Cancer (ERSPC) at 13 years of follow-up. *Lancet* **384**, 2027–2035 (2014).
25. E. Haglind *et al*.; LAPPRO steering committee, Urinary incontinence and erectile dysfunction after robotic versus open radical prostatectomy: A prospective, controlled, nonrandomised trial. *Eur. Urol.* **68**, 216–225 (2015).
26. A. R. Azzouzi *et al*., TOOKAD(®) soluble vascular-targeted photodynamic (VTP) therapy: Determination of optimal treatment conditions and assessment of effects in patients with localised prostate cancer. *BJU Int.* **112**, 766–774 (2013).
27. F. Lee *et al*., Cryosurgery for prostate cancer: Improved glandular ablation by use of 6 to 8 cryoprobes. *Urology* **54**, 135–140 (1999).
28. H. U. Ahmed *et al*., Focal therapy for localized prostate cancer: A phase I/II trial. *J. Urol.* **185**, 1246–1254 (2011).
29. S. Natarajan *et al*., Focal laser ablation of prostate cancer: Phase I clinical trial. *J. Urol.* **196**, 68–75 (2016).
30. F. Ting *et al*., Focal irreversible electroporation for prostate cancer: Functional outcomes and short-term oncological control. *Prostate Cancer Prostatic Dis.* **19**, 46–52 (2016).
31. A. Kawczyk-Krupka *et al*., Treatment of localized prostate cancer using WST-09 and WST-11 mediated vascular targeted photodynamic therapy-A review. *Photodiagn. Photodyn. Ther.* **12**, 567–574 (2015).
32. T. T. Shah *et al*., Focal cryotherapy of localized prostate cancer: A systematic review of the literature. *Expert Rev. Anticancer Ther.* **14**, 1337–1347 (2014).
33. A. Kanthabalan *et al*., Transperineal magnetic resonance imaging-targeted biopsy versus transperineal template prostate mapping biopsy in the detection of localised radio-recurrent prostate cancer. *Clin. Oncol. (R Coll. Radiol.)* **28**, 568–576 (2016).
34. L. Miao, L. Huang, Exploring the tumor microenvironment with nanoparticles. *Cancer Treat. Res.* **166**, 193–226 (2015).
35. T. J. Anchordoquy *et al*., Mechanisms and barriers in cancer nanomedicine: Addressing challenges, looking for solutions. *ACS Nano* **11**, 12–18 (2017).
36. J. A. Schwartz *et al*., Selective nanoparticle-directed ablation of the canine prostate. *Lasers Surg. Med.* **43**, 213–220 (2011).
37. K. J. Tay *et al*., Surveillance after prostate focal therapy. *World J. Urol.* **37**, 397–407 (2019).
38. FDA, FDA approval for VisualaseThermal Therapy System. https://www.accessdata.fda.gov/cdrh_docs/pdf8/K081509.pdf. Accessed 1 July 2019.
39. FDA, FDA approval for Magnetic Resonance Image Guided Laser Thermal Therapy System. https://www.accessdata.fda.gov/cdrh_docs/pdf12/K120561.pdf. Accessed 1 July 2019.
40. U. Lindner *et al*., Focal laser ablation for prostate cancer followed by radical prostatectomy: Validation of focal therapy and imaging accuracy. *Eur. Urol.* **57**, 1111–1114 (2010).
41. FDA, Magnetic Resonance-guided Laser Interstitial Thermal Therapy (MRgLITT) Devices: Letter to Health Care Providers–Risk of Tissue Overheating Due to Inaccurate Magnetic Resonance Thermometry. https://www.fda.gov/medical-devices/letters-health-care-providers/update-regarding-risk-tissue-overheating-due-inaccurate-magnetic-resonance-thermometry. Accessed 1 July 2019.
42. H. Lepor, E. Llukani, D. Sperling, J. J. Fütterer, Complications, recovery, and early functional outcomes and oncologic control following in-bore focal laser ablation of prostate cancer. *Eur. Urol.* **68**, 924–926 (2015).
43. A. Oto *et al*., MR imaging-guided focal laser ablation for prostate cancer: Phase I trial. *Radiology* **267**, 932–940 (2013).
44. S. E. Eggener, A. Yousuf, S. Watson, S. Wang, A. Oto, Phase II evaluation of magnetic resonance imaging guided focal laser ablation of prostate cancer. *J. Urol.* **196**, 1670–1675 (2016).
45. J. A. Schwartz *et al*., Feasibility study of particle-assisted laser ablation of brain tumors in orthotopic canine model. *Cancer Res.* **69**, 1659–1667 (2009).
46. A. Rastinehad, D. Siegel, P. Pinto, B. Wodo, "Template mapping biopsies: An overview of technique and results" in *Interventional Urology*, A. Rastinehad, Ed. (Springer, 2016), 119 p.